

Tidal disruption flares from stars on marginally bound and unbound orbits

Gwanwoo PARK¹ and Kimitake HAYASAKI¹

gpark@cbnu.ac.kr

Received _____; accepted _____

¹Department of Astronomy and Space Science, Chungbuk National University, Cheongju 361-763, Korea

ABSTRACT

We study the mass fallback rate of tidal disruption of a star on marginally bound and unbound orbits by a supermassive black hole (SMBH) by performing a three-dimensional smoothed particle hydrodynamic (SPH) simulations with three key parameters: the star is modeled by a polytrope with two different indexes ($n = 1.5$ and 3). The stellar orbital properties are characterized by five various orbital eccentricities ranging from $e = 0.98$ to 1.02 and five different penetration factors ranging from $\beta = 1$ to 3 , where β represents the ratio of the tidal disruption to pericenter distance radii. We analytically derive the formulae of the differential mass distributions and corresponding mass fallback rates by taking account of the three key parameters. Moreover, two critical eccentricities ($e_{\text{crit},1}$ and $e_{\text{crit},2}$) to classify tidal disruption events (TDEs) into five different types by the stellar orbit are reevaluated based on the assumption that the spread in debris energy is proportional to β^k , where k is presumed to range for $0 < k < 2$. We confirm by our SPH simulations that it ranges for $0 < k \lesssim 2$. We find that the peak of mass fallback rates is higher and its slope is steeper in the early time as the penetration factor increases for all TDE types. When the stars on marginally bound orbits with $e_{\text{crit},1} \lesssim e < 1$ (i.e., marginally eccentric TDEs) are tidally disrupted, the peak of mass fallback rates can be about one order of magnitude larger than that of parabolic TDE ($e = 1$) case. For marginally hyperbolic TDEs ($1 < e \lesssim e_{\text{crit},2}$), the mass fallback rates can be much lower than the Eddington accretion rate, which can lead to the formation of a radiatively inefficient accretion flow, while stars on hyperbolic orbits ($e \gtrsim e_{\text{crit},2}$) lead to a failed TDE. Marginally unbound TDEs could be an origin of a very low density gas disk around a dormant SMBH.

Subject headings: accretion, accretion disks – black hole physics – galaxies: nuclei
- galaxies: star clusters: general – stars: kinematics and dynamics – methods:
numerical

1. Introduction

There are growing evidences for supermassive black holes (SMBHs) that reside ubiquitously at the center of galaxies, based on observations of stellar proper motion, stellar velocity dispersion or accretion luminosity (Kormendy & Ho 2013). Tidal disruption events (TDEs) provide a distinct opportunity to probe dormant SMBHs in inactive galaxies. Once a star approaches a SMBH and enters inside the tidal sphere, the star is tidally disrupted by the SMBH. The stellar debris then falls back to the SMBH at a super-Eddington rate, leading to a prominent flaring event with a luminosity exceeding the Eddington luminosity for weeks to months (Rees 1988; Phinney 1989; Evans & Kochanek 1989).

Tidal disruption flares have been observed over the broad range of waveband from optical (van Velzen et al. 2011; Gezari et al. 2012; Holoiu et al. 2016) to ultraviolet (Gezari et al. 2006, 2008; Chornock et al. 2014) to soft X-ray (Komossa & Bade 1999; Saxton et al. 2012; Maksym et al. 2013; Auchettl et al. 2017) wavelengths with an event rate of $10^{-5} - 10^{-4}$ per year per galaxy (Donley et al. 2002; Wang & Merritt 2004; van Velzen & Farrar 2014; Stone & Metzger 2016). On the other hand, high-energy jetted TDEs have been detected through non-thermal emissions at radio (Zauderer et al. 2011; Alexander et al. 2016; van Velzen et al. 2016) and/or hard X-ray (Burrows et al. 2011; Brown et al. 2015) wavelengths with much lower event rate than the thermal TDE case (Farrar & Piran 2014). Spectroscopic studies have confirmed HI and He II (Arcavi et al. 2014) as well as metal lines (Leloudas et al. 2019). Recently discovered blue-shifted ($0.05c$) broad absorption lines are likely to result from a high velocity outflow produced by the candidate TDE AT2018zr (Hung et al. 2019).

It still remains under debate how the standard, theoretical mass fallback rate, which is proportional to $t^{-5/3}$ (Rees 1988; Phinney 1989; Evans & Kochanek 1989), can be translated into the observed light curves. While most of the soft X-ray TDEs appear to follow the

$t^{-5/3}$ power law decay curve proportional to the fallback rate (see Komossa 2015 for a review), the optical to ultraviolet TDEs exhibit the different decay curve (Gezari et al. 2012; Chornock et al. 2014; Arcavi et al. 2014; Holoien et al. 2014). There have been some arguments that the mass fallback rate itself can deviate from the $t^{-5/3}$ decay rate. Lodato et al. (2009) demonstrated that the stellar internal structure makes the mass fallback rate deviate from the standard fallback rate in an early time. When the star is simply modeled by a polytrope, the stellar density profile is characterized by a polytropic index. In this case, the polytrope index is a key parameter to determine the mass fallback rate.

The penetration factor, which is the ratio of the tidal disruption to pericenter radii, is also an important parameter for TDEs. Guillochon & Ramirez-Ruiz (2013) showed that resultant light curves can be steeper because of the centrally condensed core surviving after the partial disruption of the star. It would happen if the penetration factor is relatively low ($\beta \lesssim 2$ for the case that the polytropic index equals to 3) (Mainetti et al. 2017). The self-gravity of the survived core can change the trajectories of the striped material and therefore the resultant mass fallback rate as well (MacLeod et al. 2012). The penetration factor also plays an important role in the process of debris circularization. The energy dissipation of a strong shock by a collision between the debris head and tail naturally leads to the formation of an accretion disk (Hayasaki et al. 2013; Bonnerot et al. 2016; Hayasaki et al. 2016), although the detailed dissipation mechanism is still under debate (Stone et al. 2013; Shiokawa et al. 2015; Piran et al. 2015). Moreover, the penetration factor is a key parameter to determine the size and temperature of the circularized accretion disk (Dai et al. 2015). Recent X-ray observation suggests that the TDE would happen with very high penetration factor (Pasham et al. 2018).

In the case of tidal disruption of a star on an eccentric orbit (eccentric TDE), Hayasaki et al. (2013) found that the resultant mass fallback rate is higher with smaller orbital

eccentricity, because the fallback timescale is much shorter and more material is bound to the SMBH compared to the parabolic orbit case. In contrast, the mass fallback rate can be much smaller than the Eddington rate or even zero for a hyperbolic orbit (hyperbolic TDE) case. Hayasaki et al. (2018) proposed the five different types of TDEs are classified by two critical eccentricities, and also examined the frequency of each TDE by N-body experiments. They pointed out that stars on marginally eccentric and hyperbolic orbits can be a main TDE source in a spherical star cluster. Therefore, it is clear that the orbital eccentricity (and semi-major axis through the penetration factor) is also a key parameter to make the mass fallback rate deviate from the standard $t^{-5/3}$ decay rate.

However, there is still little known about how the three key parameters: polytropic index, penetration factor, and orbital eccentricity, and their combinations affect the mass fallback rate. In this paper, we therefore revisit the mass fallback rate onto an SMBH or IMBH by taking account of the three key parameters. In Section 2, we give a new condition to classify the TDEs by the stellar orbital type based on the assumption that the spread in debris energy is proportional to the k -th power of the penetration factor, where k is presumed to range for $0 < k < 2$ (see Stone et al. 2013). In addition, we derive analytically the formula of the mass fallback rates, which includes the effect of the three key parameters plus k on them. In Section 3, we describe our numerical simulation approach and compare the semi-analytical solutions of the mass fallback rates with the simulation results. Finally, Section 4 is devoted to the conclusion of our scenario.

2. Revisit of mass fallback rates

In this section, we revisit the mass fallback rate by taking account of a stellar density profile (Lodato et al. 2009) and the orbital eccentricity (Hayasaki et al. 2018), including the dependence of the penetration factor, $\beta = r_t/r_p$, where r_p is the pericenter distance, on a

spread in debris specific energy. As a star approaches to a SMBH or an IMBH, it is torn apart by the tidal force of the black hole, which dominates the self-gravity of the star at the tidal disruption radius:

$$r_t = \left(\frac{M_{\text{bh}}}{m_*} \right)^{1/3} r_* \approx 24 \left(\frac{M_{\text{bh}}}{10^6 M_\odot} \right)^{-2/3} \left(\frac{m_*}{M_\odot} \right)^{-1/3} \left(\frac{r_*}{R_\odot} \right) r_s. \quad (1)$$

Here we denote the black hole mass as M_{bh} , stellar mass and radius as m_* and r_* , and the Schwarzschild radius as $r_s = 2GM_{\text{bh}}/c^2$, where G and c are Newton's gravitational constant and the speed of light, respectively.

Following Stone et al. (2013), the tidal force produces a spread in specific energy of the stellar debris:

$$\Delta\mathcal{E} = \beta^k \Delta\epsilon, \quad (2)$$

where k is the power law index of the spread energy (hereafter, spread energy index), and

$$\Delta\epsilon = \frac{GM_{\text{bh}}r_*}{r_t^2} \quad (3)$$

is the standard spread energy (Rees 1988; Evans & Kochanek 1989). If $\beta = 1$ or $k = 0$, Equation (2) reduces to the standard equation. The possible range of k has been taken as $0 \leq k \leq 2$.

The mass fallback rate can be written by the chain rule as

$$\frac{dM}{dt} = \frac{dM}{d\epsilon} \frac{d\epsilon}{dt}, \quad (4)$$

where $dM/d\epsilon$ is the differential mass distribution of the stellar debris with specific energy ϵ . Because the thermal energy of the stellar debris is negligible compared with the debris binding energy, $\epsilon \approx \epsilon_d$:

$$\epsilon_d \equiv -\frac{GM_{\text{bh}}}{2a_d}, \quad (5)$$

where a_d is the semi-major axis of the stellar debris. Applying the Kepler's third law to equation (5), we obtain that

$$\frac{d\epsilon_d}{dt} = \frac{1}{3} (2\pi GM_{\text{bh}})^{2/3} t^{-5/3}. \quad (6)$$

2.1. Effect of stellar density profiles

Lodato et al. (2009) included the effect of the stellar density profile on the differential mass distribution of the stellar debris as

$$\frac{dM}{d\epsilon_d} = \frac{dM}{d\Delta r} \frac{d\Delta r}{d\epsilon_d}, \quad (7)$$

where Δr is the radial width of the star. In our case, the relation between the radial width and the debris specific binding energy is given by

$$\frac{\Delta r}{r_*} = \frac{|\epsilon_d|}{\Delta \mathcal{E}} = \frac{\mathcal{A}_c}{a_d}, \quad (8)$$

where \mathcal{A}_c is the critical semi-major axis:

$$\mathcal{A}_c = a_c \beta^{-k}, \quad (9)$$

with $a_c \equiv (M_{\text{bh}}/m_*)^{1/3} r_t/2$. If $\beta = 1$ or $k = 0$ is adopted here, equation (8) reduces to that of Lodato et al. (2009). Moreover, the radial width depends on the orbital period of the stellar debris through the binding energy, i.e., $\Delta r \propto a_d^{-1} \propto t^{-2/3}$.

The internal density structure of the star is given by the radial integral of the stellar density

$$\frac{dM}{d\Delta r} = 2\pi \int_{\Delta r}^{r_*} \rho(r) r dr, \quad (10)$$

where $\rho(r)$ is the spherically symmetric mass density of the star and the polytropes with no stellar rotation are considered. Substituting equations (8) and (10) into equation (7), we obtain the differential mass distribution as

$$\frac{dM}{d\epsilon_d} = \frac{3}{2} \left(\frac{\rho_c}{\bar{\rho}} \right) \left(\frac{r_c}{r_*} \right)^2 \left(\frac{m_*}{\Delta \mathcal{E}} \right) \int_{\Delta r/r_c}^{r_*/r_c} \theta(\xi) \xi d\xi, \quad (11)$$

where ρ_c is the central density of the star, $\bar{\rho} = m_*/(4\pi r_*^3/3)$ is the mean density of the star, r_c is the central radius of the star, and $\xi = r/r_c$ is the dimensionless radius of the star, respectively. Additionally, $\theta(\xi) = \rho/\rho_c$ is the dimensionless density of the star,

which is a function of ξ and the polytropic index, n . Because $\theta(\xi)$ is obtained by solving the Lane-Emden equation numerically, $dM/d\epsilon_d$ is semi-analytically determined (see also Figure 2). Following the Kepler’s third law, we can estimate the orbital period of the most tightly bound debris as

$$t'_{\text{mtb}} = 2\pi \sqrt{\frac{\mathcal{A}_c^3}{GM_{\text{bh}}}} = t_{\text{mtb}} \beta^{-3k/2}, \quad (12)$$

where $t_{\text{mtb}} = 2\pi\sqrt{a_c^3/GM_{\text{bh}}}$ corresponds to the $\beta = 1$ case. Substituting equations (6) and (11) into equation (4), we obtain the mass fallback rate:

$$\begin{aligned} \frac{dM}{dt} &= \left(\frac{\rho_c}{\bar{\rho}}\right) \left(\frac{r_c}{r_*}\right)^2 \left(\frac{m_*}{t'_{\text{mtb}}}\right) \left(\frac{t}{t'_{\text{mtb}}}\right)^{-5/3} \int_{\Delta r/r_c}^{r_*/r_c} \theta(\xi) \xi d\xi \\ &= \left(\frac{\rho_c}{\bar{\rho}}\right) \left(\frac{r_c}{r_*}\right)^2 \left(\frac{1}{\beta^k}\right) \left(\frac{m_*}{t_{\text{mtb}}}\right) \left(\frac{t}{t_{\text{mtb}}}\right)^{-5/3} \int_{\Delta r/r_c}^{r_*/r_c} \theta(\xi) \xi d\xi \end{aligned} \quad (13)$$

For $n = 3$ and $\xi \ll 1$, the normalized density can be expanded to be $\theta(\xi) \approx 1 - \xi^2/6 + \mathcal{O}(\xi^4)$. Since we obtain from equation (8) and (12) that $\Delta r/r_c = (r_*/r_c)(t/t_{\text{mtb}})^{-2/3}\beta^{-k}$, we can approximately estimate the mass fallback rate as $dM/dt \approx (1/2)(\rho_c/\bar{\rho})(m_*/t_{\text{mtb}})(1/\beta^k)(t/t_{\text{mtb}})^{-5/3}[1 - (t/t_{\text{mtb}})^{-4/3}\beta^{-2k}][1 - (1/12)(r_*/r_c)^2(1 - (t/t_{\text{mtb}})^{-4/3})\beta^{-2k}]$. We find that the mass fallback rate depends on not only the stellar density profile but also the penetration factor and spread energy index, which leads to the deviation from $t^{-5/3}$.

2.2. Effect of stellar orbital properties

In this section, we investigate a star that approaches the SMBH on parabolic orbit as well as eccentric and hyperbolic orbits, the specific energy of the stellar debris is in the range of $-\Delta\mathcal{E} - GM/(2a) \leq \epsilon_d \leq \Delta\mathcal{E} + GM/(2a)$, where a is the orbital semi-major axis of the approaching star.

Following Hayasaki et al. (2018), the TDEs are classified by the critical eccentricities

in terms of the orbital eccentricity of the star:

$$\left\{ \begin{array}{ll} 0 \leq e < e_{\text{crit},1} & \text{eccentric TDEs} \\ e_{\text{crit},1} \leq e < 1 & \text{marginally eccentric TDEs} \\ e = 1 & \text{parabolic TDEs} \\ 1 < e \leq e_{\text{crit},2} & \text{marginally hyperbolic TDEs} \\ e_{\text{crit},2} < e & \text{hyperbolic TDEs,} \end{array} \right. \quad (14)$$

where $e_{\text{crit},1}$ and $e_{\text{crit},2}$ are modified as

$$\begin{aligned} e_{\text{crit},1} &= 1 - 2q^{-1/3}\beta^{k-1}, \\ e_{\text{crit},2} &= 1 + 2q^{-1/3}\beta^{k-1} \end{aligned} \quad (15)$$

with $q \equiv M_{\text{bh}}/m_*$, respectively. If $\beta = 1$ or $k = 0$, these two terms reduce to the previously defined critical eccentricities (see equations (5) and (6) of Hayasaki et al. 2018). The modified specific binding energy of the most tightly bound stellar debris for eccentric or hyperbolic stellar orbits is given by

$$\epsilon_{\text{mtb}} = -\Delta\mathcal{E} \pm \frac{GM_{\text{bh}}}{2a} = -\left(1 \mp \frac{\mathcal{A}_c}{a}\right)\Delta\mathcal{E}, \quad (16)$$

where the negative and positive signs of the specific orbital energy of the star indicate the eccentric and hyperbolic orbit cases, respectively. The orbital period of the most tightly bound debris is also changed as

$$\tau_{\text{mtb}} = 2\pi\sqrt{\frac{\mathcal{A}_c^3}{GM_{\text{bh}}}}\left(1 \mp \frac{\mathcal{A}_c}{a}\right)^{-3/2} = t_{\text{mtb}}(\beta^{-3k/2})\left(1 \mp \frac{\mathcal{A}_c}{a}\right)^{-3/2}, \quad (17)$$

where we use equation (12) and \mathcal{A}_c/a should be smaller than unity for the upper negative sign (hyperbolic TDE) case. The differential mass distribution is thus changed from equation (11) to

$$\frac{dM}{d\epsilon_d} = \frac{3}{2}\left(\frac{\rho_c}{\bar{\rho}}\right)\left(\frac{r_c}{r_*}\right)^2\left(\frac{m_*}{\Delta\mathcal{E}}\right)\int_{\Delta r'/r_c}^{r_*/r_c}\theta(\xi)\xi d\xi, \quad (18)$$

where $\Delta r'$ is the newly defined radial width of the star and is given by

$$\frac{\Delta r'}{r_*} = \frac{|\epsilon_d|}{\Delta \mathcal{E}} = \frac{\mathcal{A}_c}{a_d} \left(1 \mp \frac{a_d}{a} \right) \quad (19)$$

with the modification of the debris binding energy, i.e., $\epsilon_d = -GM/(2a_d) \pm GM/(2a)$. Note that $\theta(\xi) = 0$ if $\Delta r'/r_*$ is greater than unity because there is no stellar gas there.

Substituting equations (6) and (18) into equation (4) and applying equations (16) and (17), we can obtain the modified mass fallback rate as

$$\begin{aligned} \frac{dM}{dt} &= \left(\frac{\rho_c}{\bar{\rho}} \right) \left(\frac{r_c}{r_*} \right)^2 \left(1 \mp \frac{\mathcal{A}_c}{a} \right) \left(\frac{m_*}{\tau_{\text{mtb}}} \right) \left(\frac{t}{\tau_{\text{mtb}}} \right)^{-5/3} \int_{\Delta r'/r_c}^{r_*/r_c} \theta(\xi) \xi d\xi. \\ &= \left(\frac{\rho_c}{\bar{\rho}} \right) \left(\frac{r_c}{r_*} \right)^2 \left(\frac{1}{\beta^k} \right) \left(\frac{m_*}{t_{\text{mtb}}} \right) \left(\frac{t}{t_{\text{mtb}}} \right)^{-5/3} \int_{\Delta r'/r_c}^{r_*/r_c} \theta(\xi) \xi d\xi. \end{aligned} \quad (20)$$

Applying $\theta(\xi) \simeq 1 - \xi^2/6 + O(\xi^4)$ to equation (20) for the $n = 3$ and $\xi \ll 1$ case, we approximately estimate the mass fallback rate as $dM/dt \approx (\rho_c/\bar{\rho})(m_*/t_{\text{mtb}})(1/\beta^k)(t/t_{\text{mtb}})^{-5/3}[1 - (t/t_{\text{mtb}})^{-4/3}\beta^{-2k}(1 \pm (t/t_{\text{mtb}})^{2/3}(a_c/a))^2][1 - (1/12)(r_*/r_c)^2(1 - (t/t_{\text{mtb}})^{-4/3}\beta^{-2k}(1 \pm (t/t_{\text{mtb}})^{2/3}(a_c/a))^2)]$, where the positive and negative signs represent the eccentric and hyperbolic orbit cases, respectively. We find that the dependence of the mass fallback rate on the orbital semi-major axis, the penetration factor, and the spread energy index leads to the deviation from $t^{-5/3}$. We test this hypothesis by numerical simulations and describe our results in Section 3.

2.3. Numerical simulations

We evaluate how well the analytical solution matches the numerical simulations by using a three-dimensional (3D) Smoothed Particle Hydrodynamics (SPH) code. The SPH code is developed based on the original version of Benz (1990); Benz et al. (1990) and substantially modified as described in Bate et al. (1995) and parallelized using both OpenMP and MPI.

Two-stage simulations are performed to model a tidal interaction between a star and a black hole. In the first-stage simulation, we model the star by a polytrope with $n = 1.5$ and $n = 3$ for a solar-type star. We run the simulations until the polytrope is virialized. In the second-stage simulation, the star is initially located at a distance of three times the tidal disruption radii and approaches the SMBH following Kepler’s third law for five different orbital eccentricities and five different penetration factors per each orbital eccentricity. In summary, we run a total 50 simulations in the second-stage. The stellar mass, stellar radius, and black hole mass are held constant throughout the simulations at $m_* = 1 M_\odot$, $r_* = 1 R_\odot$, and $M_{\text{bh}} = 10^6 M_\odot$, respectively. The total number of SPH particles used in each simulation is slightly more than 10^6 and the run time is measured in units of $\Omega_*^{-1} = \sqrt{r_*^3/(Gm_*)} \simeq 1.6 \times 10^3$ s.

Tables 1 and 2 present a summary of the SPH simulation models and the corresponding spread energy indices obtained from the simulations. For both tables, the first to third columns show the polytropic index (n), the penetration factor (β), and the orbital eccentricity (e), respectively. The fourth and fifth columns show two critical eccentricities $e_{\text{crit},1}$ and $e_{\text{crit},2}$, respectively (see equation 15). The final column presents the spread energy index (k), which is estimated by fitting the simulation data (see the detail in Section 3.2). We find from Tables 1 and 2 that the $e = 0.98$ and $e = 0.99$, $e = 1.0$, $e = 1.01$, and $e = 1.02$ cases correspond to marginally eccentric, parabolic, marginally hyperbolic, hyperbolic TDEs, respectively.

Table 1: Summary for parameters of our simulations. The first column shows the polytrope index (n). The second and third columns present the penetration factor (β) and the orbital eccentricity (e), respectively. The fourth and fifth columns show the two critical eccentricities $e_{\text{crit},1}$ and $e_{\text{crit},2}$, respectively (see equation 15). The final column presents the specific energy index (k), which is obtained by fitting the simulation data (see equation 21 and also Figures 7 and 8).

n	β	e	$e_{\text{crit},1}$	$e_{\text{crit},2}$	k	n	β	e	$e_{\text{crit},1}$	$e_{\text{crit},2}$	k	
		1	0.980	1.02	–			1	0.980	1.02	–	
		1.5	0.983	1.02	0.595			1.5	0.983	1.02	0.584	
1.5	2	0.98	0.987	1.01	0.332	1.5	2	1.01	0.988	1.01	0.317	
		2.5	0.989	1.01	0.293			2.5	0.989	1.01	0.275	
		3	0.982	1.02	0.902			3	0.991	1.01	0.318	
		1	0.980	1.02	–			1	0.980	1.02	–	
		1.5	0.983	1.02	0.593			1.5	0.983	1.02	0.580	
1.5	2	0.99	0.987	1.00	0.327	1.5	2	1.02	0.988	1.01	0.312	
		2.5	0.989	1.01	0.287			2.5	0.989	1.01	0.270	
		3	0.982	1.02	0.897			3	0.991	1.01	0.313	
		1	0.980	1.02	–			1	0.980	1.02	–	
		1.5	0.983	1.02	0.646			1.5	0.983	1.02	0.580	
1.5	2	1.0	0.987	1.01	0.324			2	1.02	0.988	1.01	0.312
		2.5	0.989	1.01	0.273			2.5	0.989	1.01	0.270	
		3	0.990	1.01	0.323			3	0.991	1.01	0.313	

Table 2: Summary for parameters of our simulations. The format of each column is the same as Table 1, but for the $n = 3$ case.

n	β	e	$e_{\text{crit},1}$	$e_{\text{crit},2}$	k	n	β	e	$e_{\text{crit},1}$	$e_{\text{crit},2}$	k
	1		0.980	1.02	–		1		0.980	1.02	–
	1.5		0.968	1.03	2.17		1.5		0.969	1.03	2.10
3	2	0.98	0.970	1.03	1.58	3	2	1.01	0.971	1.03	1.56
	2.5		0.976	1.02	1.19		2.5		0.976	1.02	1.19
	3		0.980	1.02	0.981		3		0.981	1.02	0.971
	1		0.980	1.02	–		1		0.980	1.02	–
	1.5		0.968	1.03	2.14		1.5		0.969	1.03	2.07
3	2	0.99	0.970	1.03	1.57	3	2	1.02	0.971	1.03	1.55
	2.5		0.976	1.02	1.19		2.5		0.976	1.02	1.18
	3		0.980	1.02	0.978		3		0.981	1.02	0.967
	1		0.980	1.02	–		1		0.980	1.02	–
	1.5		0.968	1.03	2.12		1.5		0.969	1.03	2.07
3	2	1.0	0.970	1.03	1.57	3	2	1.02	0.971	1.03	1.55
	2.5		0.976	1.02	1.19		2.5		0.976	1.02	1.18
	3		0.981	1.02	0.974		3		0.981	1.02	0.967

3. Results

In this section, we describe the simulation results in order to compare our semi-analytical prediction with that of the SPH simulations.

3.1. Differential mass distribution of stellar debris

We first compare the simulated differential mass distribution of the stellar debris over the specific energy measured at a run time of $t = 4$ with the Gaussian-fitted distributions; we then compare our findings with the semi-analytical solution given by equation (20). The relevance of the fitting is also discussed.

Figure 1 shows the dependence of the differential debris mass distribution on the normalized specific energy for $n = 1.5$ with five different penetration factors. Panel (a) shows the differential mass distribution for the standard, parabolic case ($e = 1.0$). Panels (b)-(e) show results for the marginally eccentric ($e = 0.98$ and 0.99) and marginally hyperbolic ($e = 1.01$ and $e = 1.02$) TDE cases, respectively. In all the panels, the red, green, blue, magenta, and brown color points are the differential mass distributions for $\beta = 1$, $\beta = 1.5$, $\beta = 2$, $\beta = 2.5$, and $\beta = 3$, respectively. The corresponding fitted curves are obtained using the *FindFit* model provided by *Mathematica* and are represented in the same color format. It can find a non-linear fitting with the gaussian function, $f(x) = (1/\sqrt{2\pi}\sigma) \exp[-(1/2)([x - \mu]/\sigma)^2]$, where μ is the position of the center of the peak and σ is the standard deviation which is proportional to a half width at half maximum (HWHM). We also simply evaluate the accuracy of the fitting by using the root mean square (RMS) and its square is given by $\text{RMS}^2 = \sum_{i=1}^{N_d} ([y_i - f(x_i)]/f(x_i))^2/N_d$, where N_d is the number of data points, and x_i and y_i are the normalized specific energy at the i -th data point and the corresponding differential mass distribution, respectively. We confirm

that for parabolic TDEs, the differential mass is distributed around a specific energy of zero and also a half of the debris mass, independently of β , is bound by the SMBH. As we predicted in Section 2.2, the position of the peak of the differential mass is shifted in the negative direction for eccentric TDEs and the resultant differential mass is distributed over there, while the position of the peak is positively shifted for the hyperbolic TDE cases. The deviation of the peak position corresponds to a_c/a to an accuracy of less than 2%. Most of the debris mass can fallback to the SMBH because of their negative binding energy in marginally eccentric TDEs, whereas most of the debris mass moves far away from the SMBH because of their positive binding energy in marginally hyperbolic TDE case. The debris mass becomes more widely distributed for the debris specific energy as the penetration factor increases, particularly for the marginally eccentric and hyperbolic TDEs. In all cases, the peak of the differential mass distribution is smaller as the penetration factor is larger.

Figure 2 is the same format as Figure 1 but for the $n = 3$ case. For the parabolic TDEs, a half of stellar debris is bound, whereas other half is unbound to the SMBH. The differential mass distributions for $\beta = 2$, $\beta = 2.5$, and $\beta = 3$ are similar as those of $n = 1.5$, while the distribution of $\beta = 1$ is steeper than that of $n = 1.5$ because the central density of $n = 3$ polytrope is one order magnitude higher than $n = 1.5$ case, leading to the partial disruption of the star. This tendency appears to be independent of the orbital eccentricity.

Figure 3 depicts the penetration factor dependence of the RMS between the simulated data points and the Gaussian-fitted curves. Panels (a) and (b) represent the $n=1.5$ and the $n=3$ cases, respectively. We see from panel (a) that the maximum RMS value is $\sim 18\%$ at $\beta = 1.5$, whereas the maximum RMS value is less than 5% at $\beta = 2.5$. As shown in panel (b), the maximum RMS value is $\sim 24\%$ at $\beta = 2.0$, whereas the maximum RMS value is less than 7% at $\beta = 1.0$. We also find that the RMS does not depend on the orbital

eccentricity for the $n = 1.5$ and $n = 3$ cases. Figures 4 and 5 show the comparison between the Gaussian-fitted curves with the semi-analytic solutions with $n = 1.5$ and $n = 3$, which is given by equation (20), respectively. We find from the figures that the simulated curves are good agreement with the semi-analytical solutions.

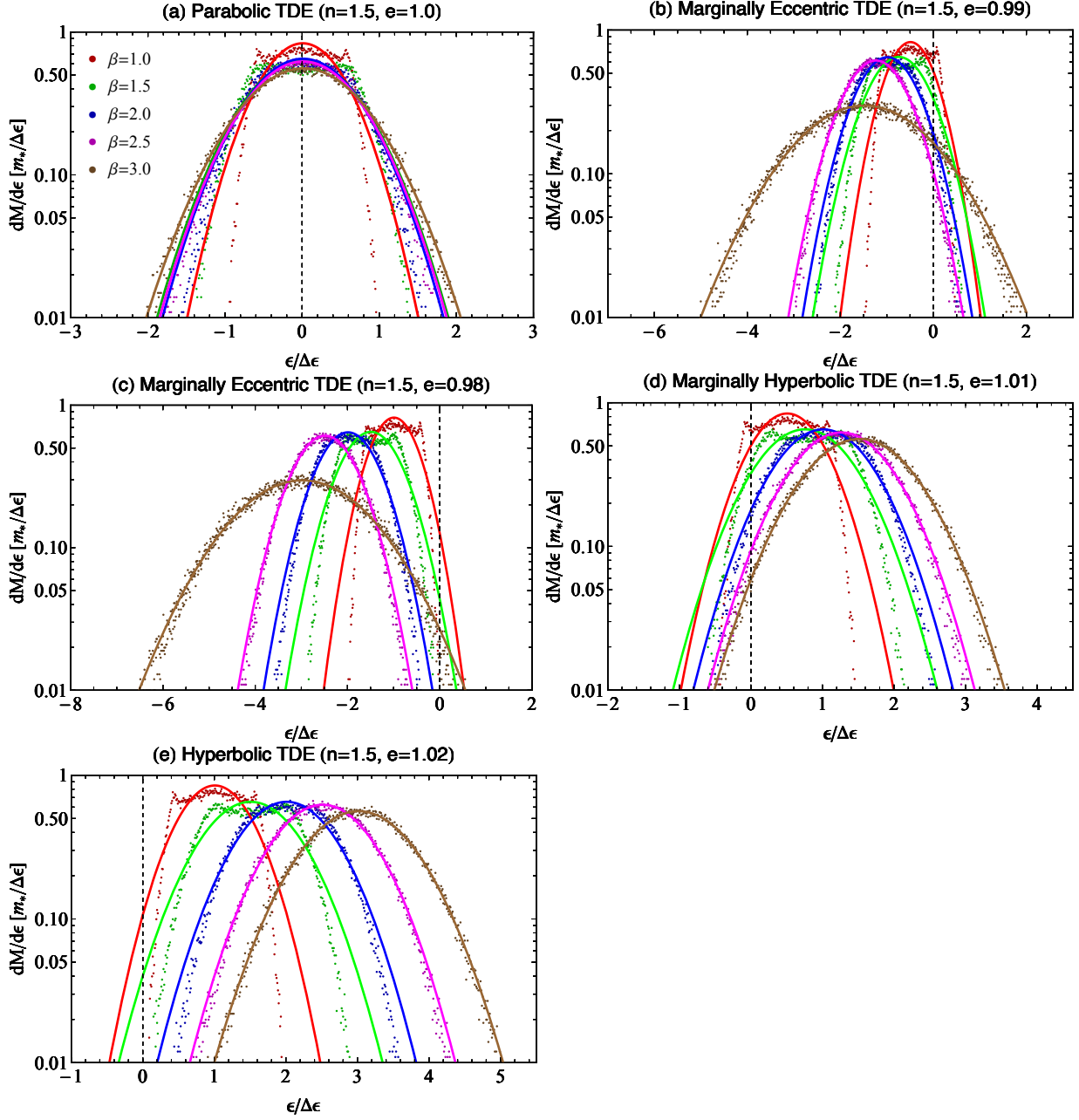


Fig. 1.— Simulated differential mass distributions of the stellar debris over the specific energy in units of $m_*/\Delta\epsilon$, for the case of $n = 1.5$ with five different orbital eccentricities. In each panel, the red, green, blue, magenta, and brown solid lines show the corresponding Gaussian-fitted light curves for $\beta = 1, 1.5, 2, 2.5$ and 3 , respectively.

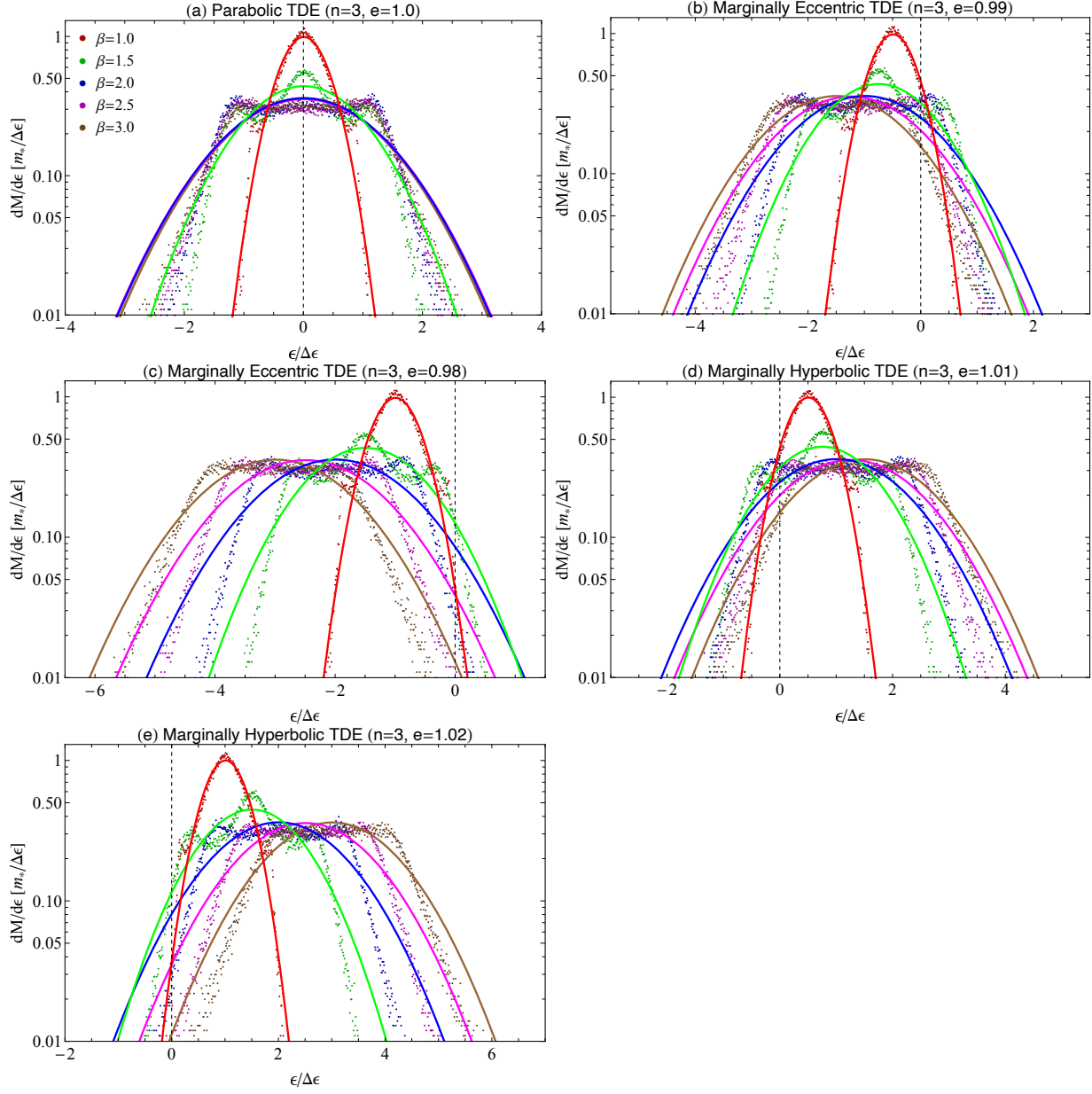


Fig. 2.— The same format as Figure 1, but for the case of $n = 3$

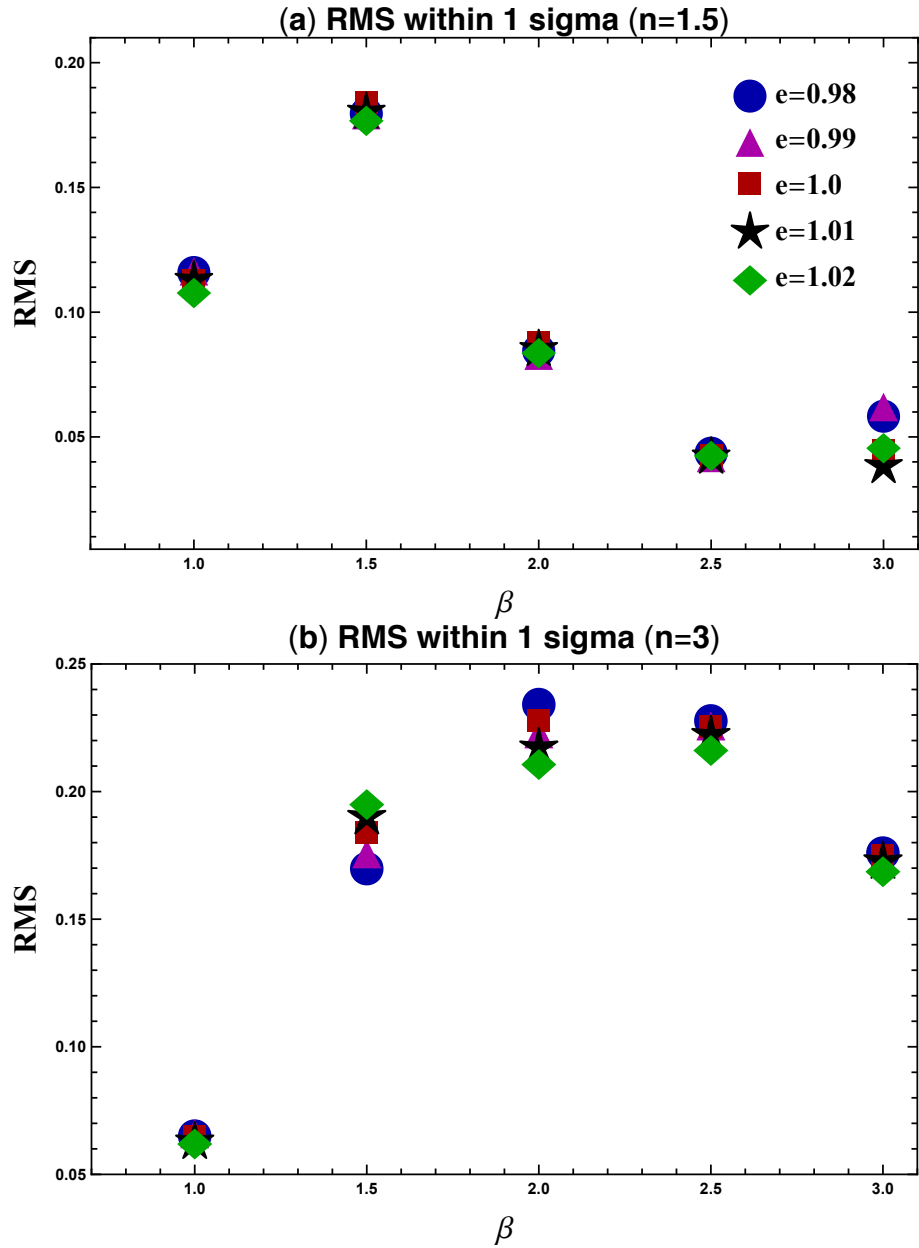


Fig. 3.— The root-mean square (RMS) between simulated data points and the Gaussian-fitted curves. Panels (a) and (b) shows results for $n = 1.5$ and $n = 3$, respectively.

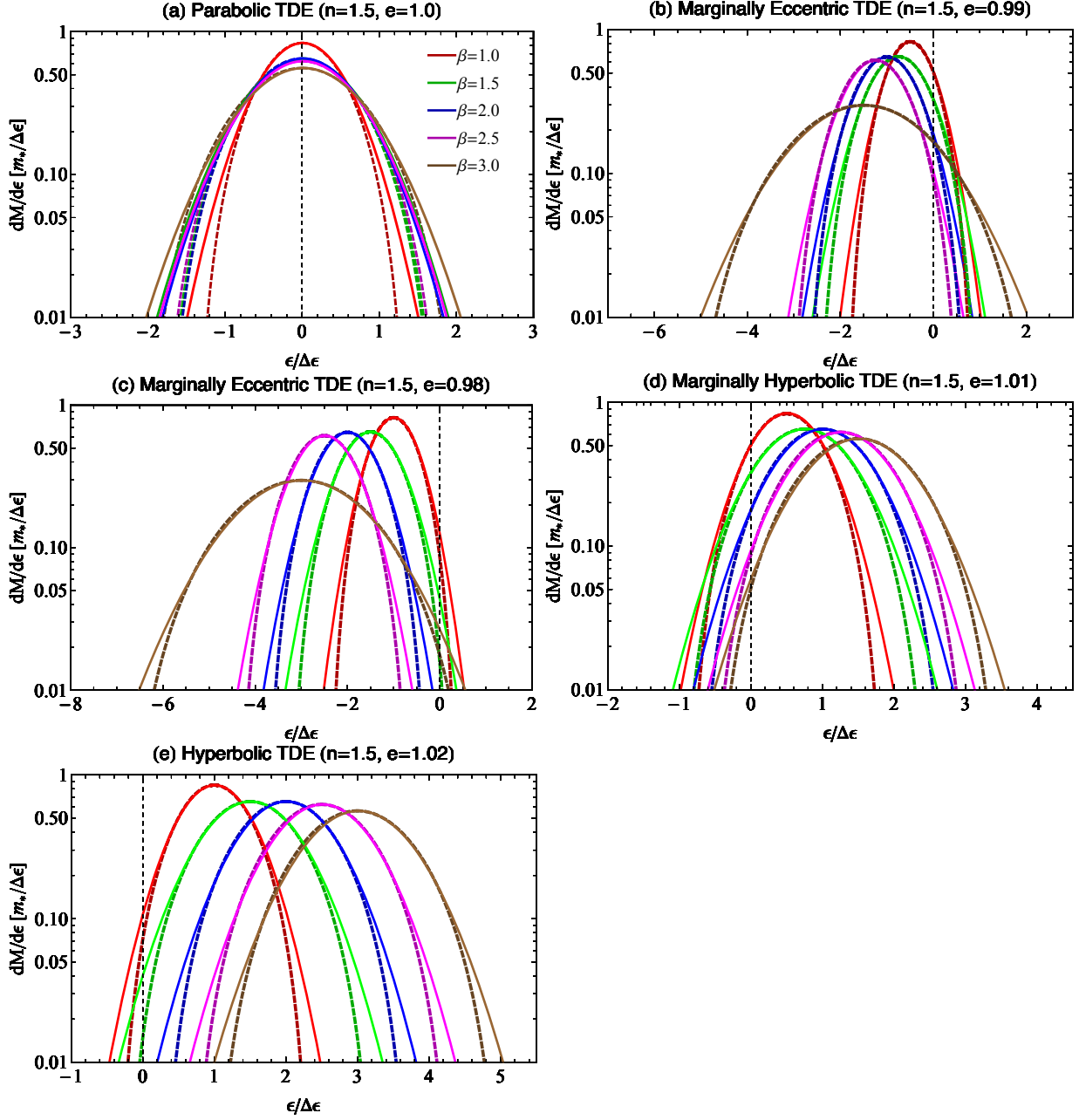


Fig. 4.— Comparison between the Gaussian-fitted curves of the simulated differential mass distributions and the corresponding semi-analytical solutions, for the case of $n = 1.5$ with five different orbital eccentricities. The solid and dashed lines show the Gaussian-fitted curves and the semi-analytical solutions, respectively. The color format of each line is the same as that of Figure 1.

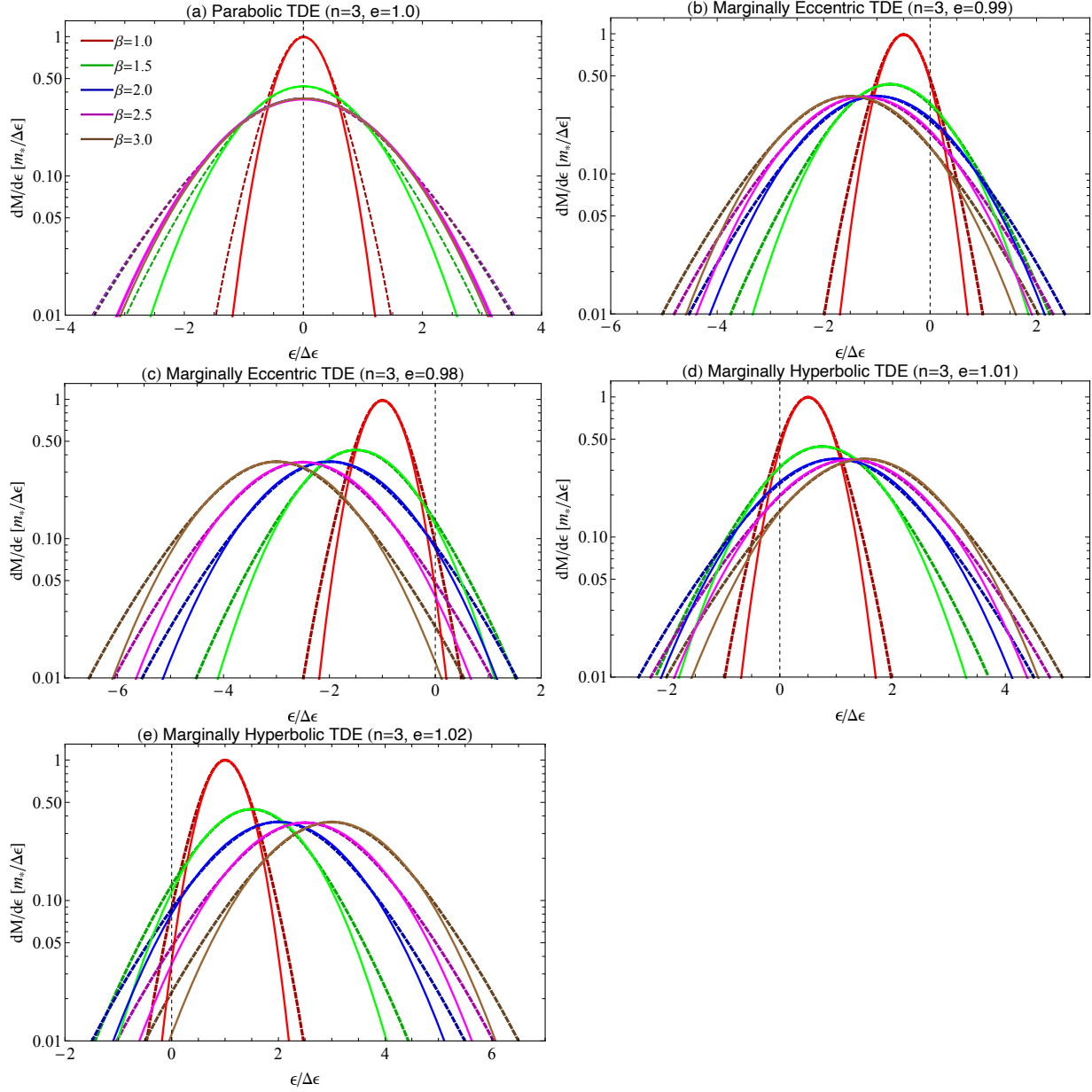


Fig. 5.— The same format as Figure 2, but for the case of $n = 3$

3.2. Evaluation of k

Assuming that the standard deviation of the Gaussian-fitted curve, $\Delta\mathcal{E}_{\text{sim}}$, corresponds to the analytical spread energy $\Delta\mathcal{E}$, we can evaluate the spread energy index from equation (2) by

$$k = \frac{\log(\Delta\mathcal{E}_{\text{sim}}/\Delta\epsilon)}{\log \beta}. \quad (21)$$

Figure 6 shows the dependence of the simulated spread energy on the penetration factor. Panels (a) and (b) show β -dependence of $\Delta\mathcal{E}_{\text{sim}}/\Delta\mathcal{E}$ for the $n = 1.5$ and $n = 3$ cases, respectively. Panels (c) and (d) depict β -dependence of $\Delta\mathcal{E}_{\text{sim}}/\Delta\epsilon$ for the $n = 1.5$ and $n = 3$ cases, respectively. In each panel, the blue circles, magenta triangles, red squares, black stars and green rhombuses represent results of $e = 0.98, 0.99, 1.0, 1.01$ and 1.02 , respectively. We find from panels (a) and (b) that the simulated spread energies are in good agreement with the analytical values for the $n = 1.5$ and $n = 3$ cases, although the error of 2% is obtained for $\beta = 1$. In addition, $\Delta\mathcal{E}_{\text{sim}}/\Delta\epsilon$ slightly increases for $\beta = 1$ as the orbital eccentricity decreases. We also find from panels (c) and (d) that the simulated spread energy, overall, increases beyond $\Delta\epsilon$ as the penetration factor increases.

Figures 7 and 8 depict the dependence of $\Delta\mathcal{E}_{\text{sim}}/\Delta\mathcal{E}$ on the spread energy index k with different penetration factors for the $n = 1.5$ and $n = 3$ cases, respectively. Panels (a) to (d) show results for $\beta = 1.5, \beta = 2, \beta = 2.5$, and $\beta = 3$, respectively. These two figures show that the value of k is distributed between 0.2 and 0.9 for $n = 1.5$, while the value of k takes between 0.95 and 2.2 for the $n = 3$ case. The detailed values of k can be seen at the sixth column of Tables 1 and 2. We also find that the value of k is larger than 2 only for the $\beta = 1.5$ and $n = 3$ case.

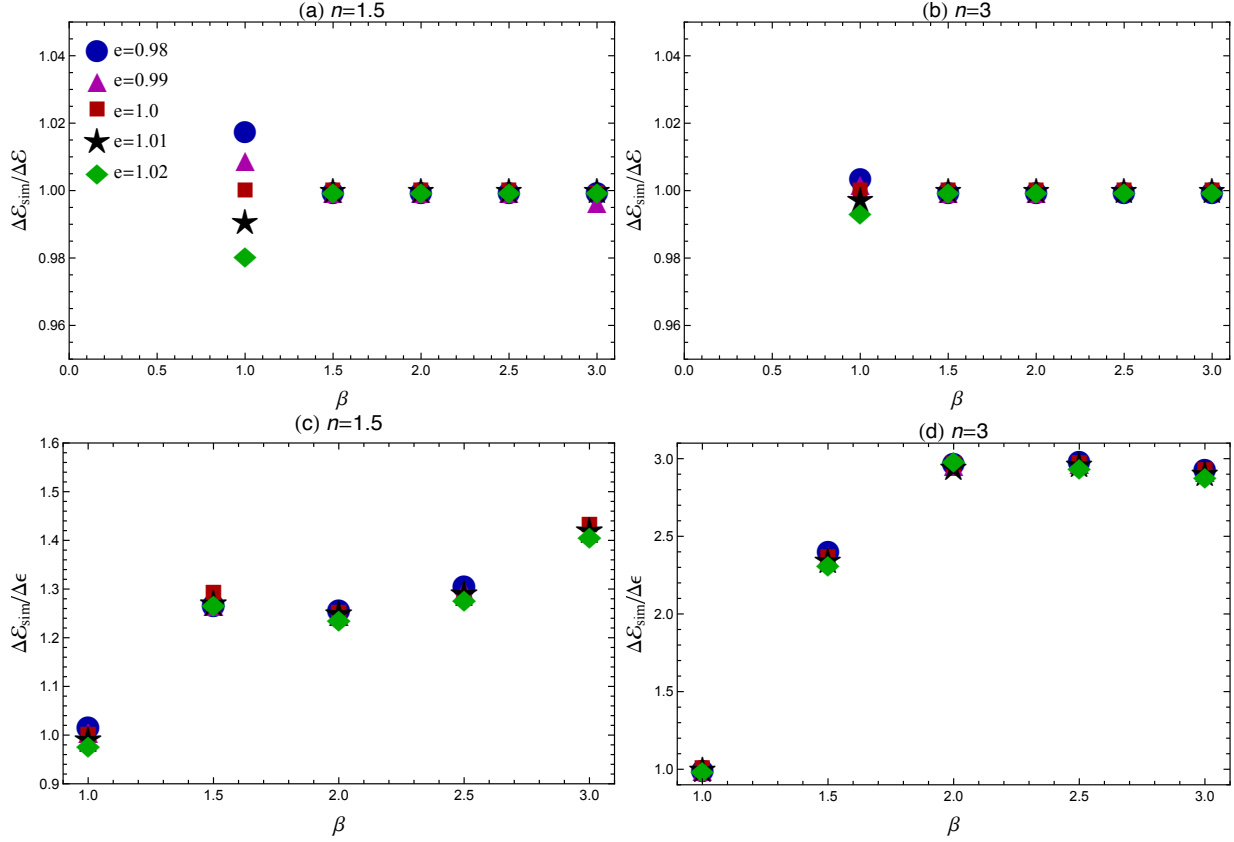


Fig. 6.— Dependence of the simulated spread energy on the penetration factor. Panels (a) and (b) show β -dependence of $\Delta\mathcal{E}_{\text{sim}}/\Delta\mathcal{E}$ for the $n = 1.5$ and $n = 3$ cases, respectively. Panels (c) and (d) depict β -dependence of $\Delta\mathcal{E}_{\text{sim}}/\Delta\epsilon$ for the $n = 1.5$ and $n = 3$ cases, respectively. Note that the relation between respective normalization is given by $\Delta\mathcal{E} = \Delta\epsilon \beta^k$ (see also equation 2). In each panel, the blue circles, magenta triangles, red squares, black stars, and green rhombuses represent results for $e = 0.98, 0.99, 1.0, 1.01$ and 1.02 , respectively.

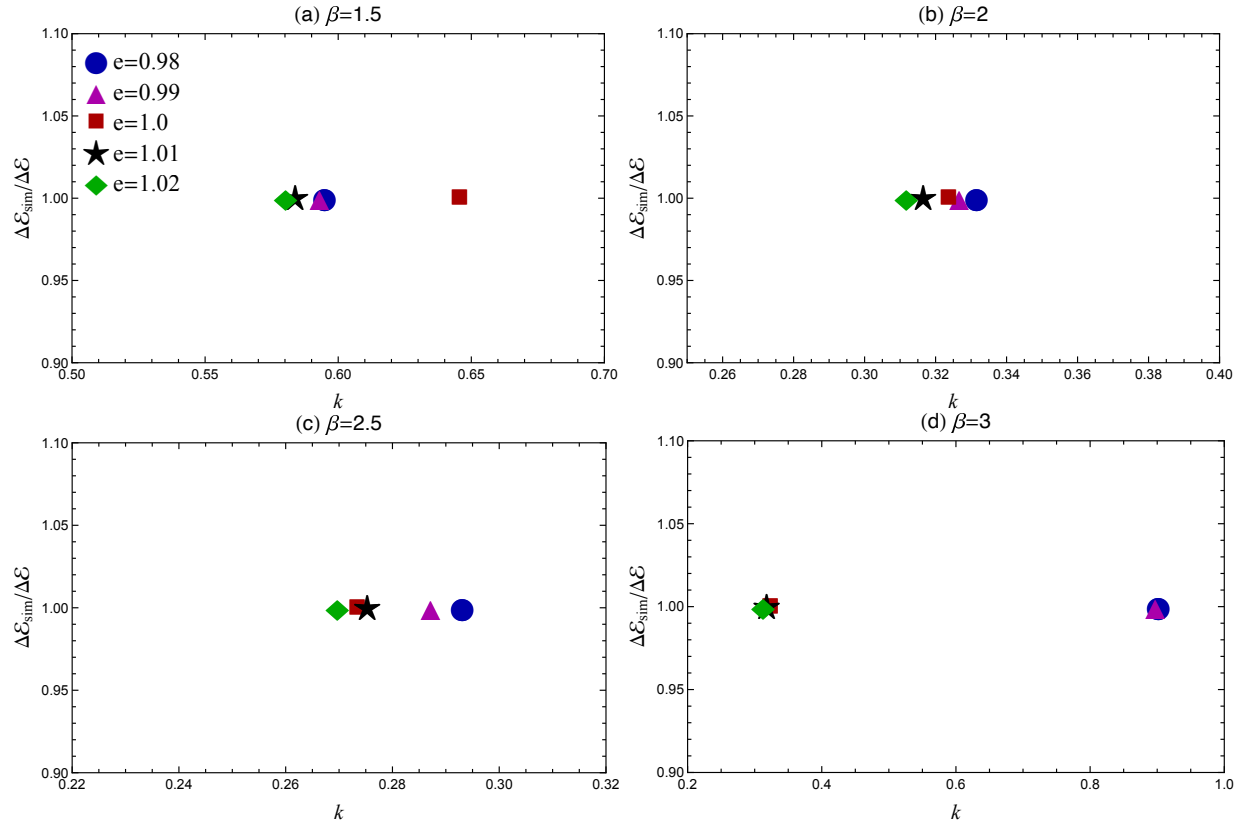


Fig. 7.— Dependence of $\Delta\mathcal{E}_{\text{sim}}/\Delta\mathcal{E}$ on the spread energy index with four different penetration factors for the $n = 1.5$ case. The blue circles, magenta triangles, red squares, black stars, and green rhombuses represent results for $e = 0.98, 0.99, 1.0, 1.01$ and 1.02 , respectively.

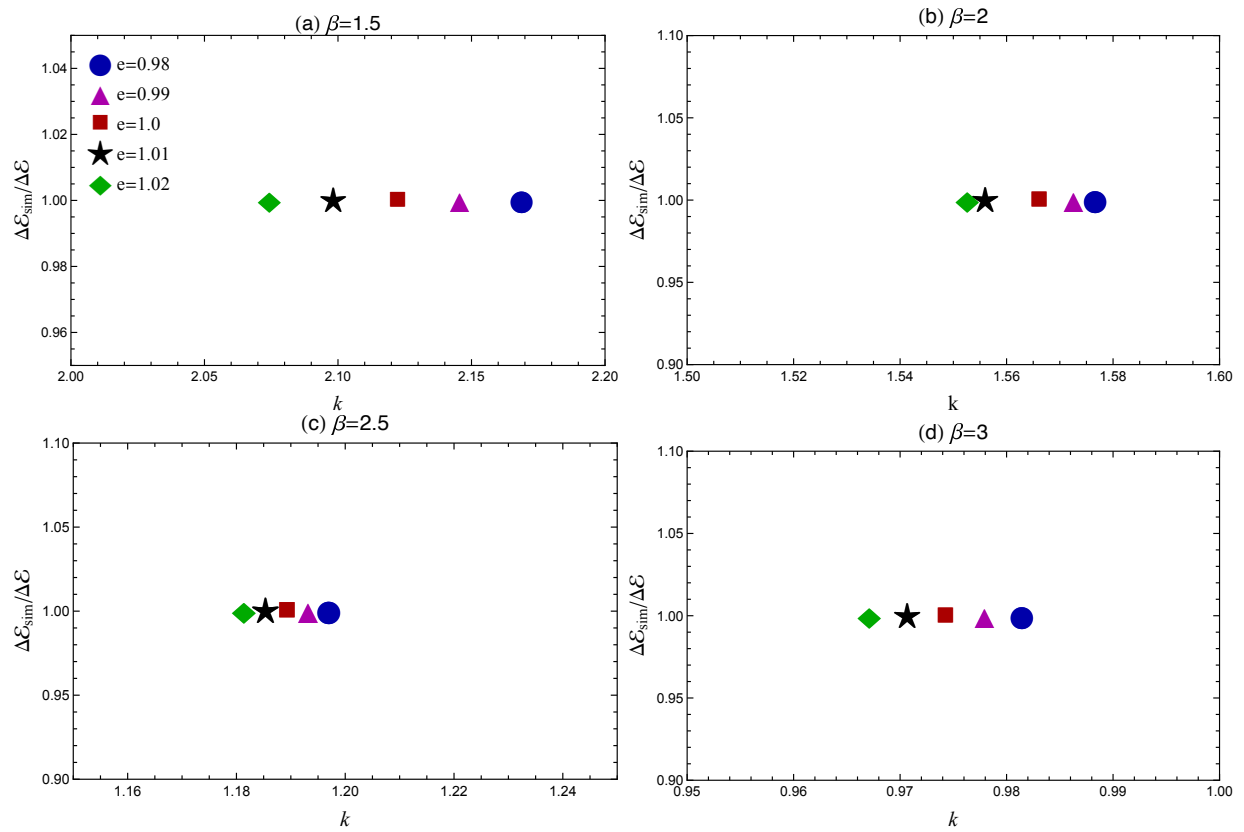


Fig. 8.— The same format as Figure 7, but for the case of $n = 3$.

3.3. Mass fallback rates

In this section, we evaluate the mass fallback rate of each model by analyzing the hydrodynamic simulation results. Figure 9 shows the penetration factor dependence of the slope of the mass fallback rates. Assuming that $dM/dt \propto t^{-s}$, where s is the power-law index of time, we can evaluate s by using the power-law fitting in the range of $1.5\tau_{\text{mtb}} \leq t \leq 10\tau_{\text{mtb}}$. Panels (a) and (b) show results for $n = 1.5$ and $n = 3$, respectively. The blue circle, magenta triangle, red square, and black star represent the slopes of $e = 0.98$, $e = 0.99$, $e = 1.0$, and $e = 1.01$ cases, respectively. We also find that the parabolic ($e = 1.0$) and marginally hyperbolic ($e = 1.01$) TDEs signify a shallower decay rate than $t^{-5/3}$ for both $n = 1.5$ and $n = 3$. In contrast, the marginally eccentric ($e = 0.99$) TDE shows the steeper decay rate than $t^{-5/3}$ if $\beta \geq 1.5$. This trend indicates that the penetration factor positively correlates with the slope of mass fallback rate if the orbital eccentricity ranges between $e_{\text{crit},1}$ and 1.0.

Figure 10 depicts the simulated mass fallback rates for $n = 1.5$, which are normalized by $m_*/t_{\text{tmb}} = 0.11 M_{\odot}/\text{yr} (M_{\text{bh}}/10^6 M_{\odot})^{-1/2} (M_*/M_{\odot}) (r_*/R_{\odot})^{-3/2} (\beta/1)^{3k/2}$, where the value of k is obtained from Table 1. The red and blue curves show results for $\beta = 1$ and 2.5, respectively, and the dashed line denotes the normalized Eddington accretion rate. Panels (a)-(d) depict the mass fallback rate of the parabolic TDE ($e = 1.0$), marginally eccentric TDEs ($e = 0.99$ and $e = 0.98$), and marginally hyperbolic TDEs ($e = 1.01$), respectively. The figures show that the mass fallback rate for $\beta = 2.5$ is steeper than the $\beta = 1$ case in the early phase of all TDE types (parabolic, marginally eccentric and marginally hyperbolic TDEs). The mass fallback rate of marginally eccentric TDEs is about one order of magnitude larger than that of the parabolic ($e = 1.0$) TDE, while that of the marginally hyperbolic ($e = 1.01$) TDE is less than the Eddington rate and about one order of magnitude smaller than that of the parabolic TDE.

Figure 11 is the same format as Figure 10, but for $n = 3$. The mass fallback rates are normalized by $m_*/t_{\text{mtb}} = 0.11 M_\odot/\text{yr} (M_{\text{bh}}/10^6 M_\odot)^{-1/2} (M_*/M_\odot) (r_*/R_\odot)^{-3/2} (\beta/1)^{3k/2}$, where the value of k is obtained from Table 2. The peak of the mass fallback rate for $n = 3$ is larger than that of the $n = 1.5$ case for all TDE types. Moreover, for $n = 1.5$, the mass fallback rate of the $\beta = 3$ case is steeper than that of the $\beta = 1$ case in the early phase. The Eddington accretion rate is given by $\dot{M} = L_{\text{Edd}}/(\eta c^2)$, where L_{Edd} is the Eddington luminosity and η is the mass-to-energy conversion efficiency. Equating the Eddington accretion rate with equation 20, we obtain the duration of a super-Eddington accretion phase:

$$t_{\text{Edd}} = t_{\text{mtb}} \left(\frac{L_{\text{Edd}}}{\eta c^2} \right)^{-3/5} \left(\frac{\rho_c}{\bar{\rho}} \right)^{3/5} \left(\frac{r_c}{r_*} \right)^{6/5} \left(\frac{m_*}{t_{\text{mtb}}} \right)^{3/5} \left(\int_{\Delta r'/r_c}^{r_*/r_c} \theta(\xi) \xi d\xi \right)^{3/5} \beta^{-3k/5}. \quad (22)$$

Thus, the duration is shorter as the penetration factor is higher as far as k is positive. We confirm from Figures 10 and 11 that the negative correlation between the duration and the penetration factor is consistent with the SPH simulation results. These findings demonstrate that the shorter duration can be evidence for the higher- β TDEs.

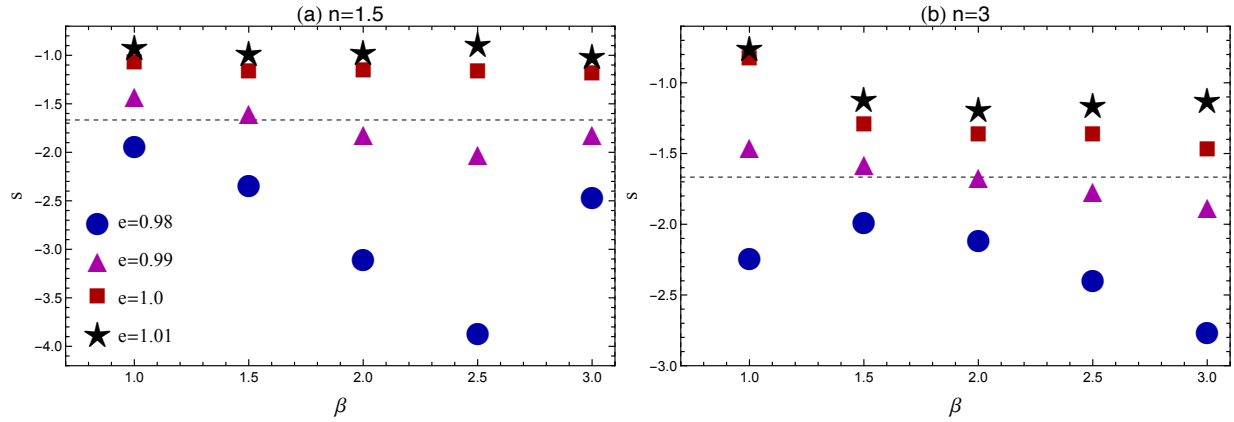


Fig. 9.— Penetration factor dependence of the slope of the mass fallback rates. We assume $dM/dt \propto t^{-s}$, where s is the power-law index of time. Panels (a) and (b) show results for $n = 1.5$ and $n = 3$, respectively. The blue circles, magenta triangles, red squares, and black stars denote the slopes of $e = 0.98$, $e = 0.99$, $e = 1.0$, and $e = 1.01$, respectively.

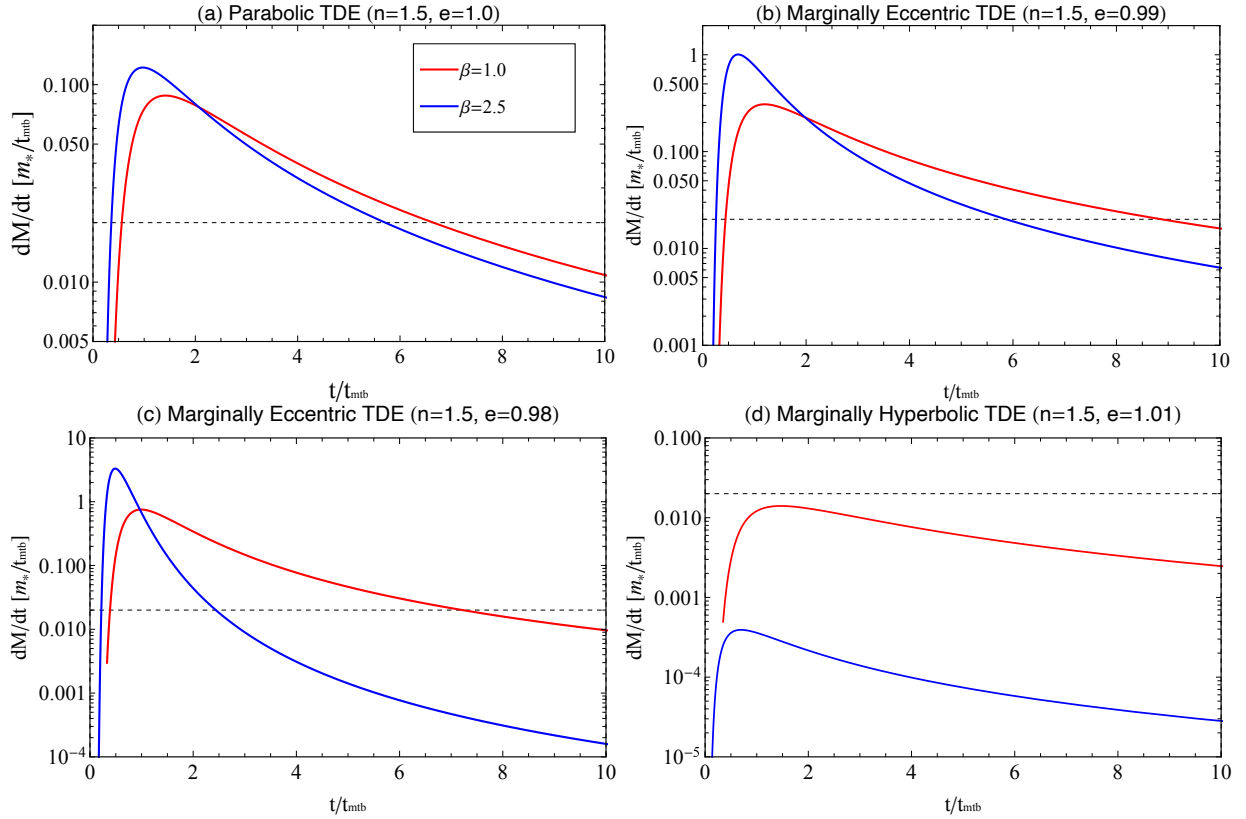


Fig. 10.— Simulated mass fallback rates, which are normalized by $m_*/t_{\text{tmb}} = 0.11M_{\odot}/\text{yr} (M_{\text{bh}}/10^6 M_{\odot})^{-1/2} (M_*/M_{\odot}) (r_*/R_{\odot})^{-3/2} (\beta/1)^{3k/2}$, in the case of $n=1.5$. The red and blue curves show results for $\beta = 1$ and 2.5 , respectively. The dashed line represents the normalized Eddington accretion rate. Panels (a)-(d) depict the mass fallback rate of the parabolic TDE ($e = 1.0$), marginally eccentric TDEs ($e = 0.99$ and $e = 0.98$), and marginally hyperbolic TDEs ($e = 1.01$), respectively.

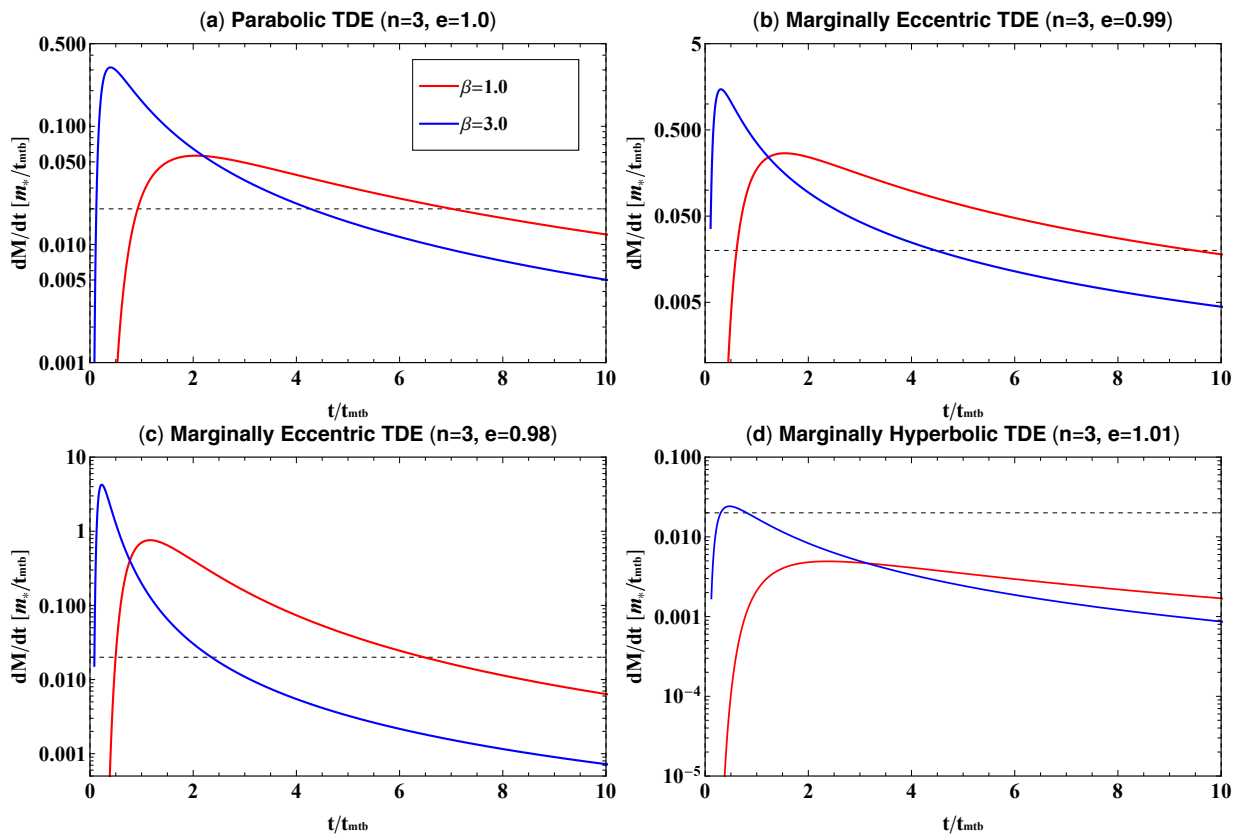


Fig. 11.— The same format as Figure 10, but for $n = 3$ and both $\beta = 1$ and $\beta = 3$.

4. Discussion and Conclusions

We have revisited the mass fallback rates by taking account of the penetration factor (β), orbital eccentricity (e), and stellar density profile (n). We have compared the semi-analytical solutions with 3D SPH simulation results. Our primary conclusions are summarized as follows:

1. We have analytically derived the formulations of both the differential mass distribution and corresponding mass fallback rate and obtained the semi-analytical solutions for them. Both the differential mass distribution and corresponding mass fallback rate depend on the penetration factor, spread energy index, orbital semi-major axis, and stellar density profile (see equations 11 and 18 for differential mass distributions and equations 13 and 20 for mass fallback rates).
2. The differential mass distributions obtained by the SPH simulations show good agreement with the Gaussian-fitted curves, within errors of $\sim 5\%$ to 18% for $n = 1.5$, and $\sim 7\%$ to 24% for $n = 3$. We find that the Gaussian-fitted curves are in substantially good agreement with the semi-analytical solutions, indicating that the analytically derived mass fallback rates match the simulated rates within the range of the fitting accuracy.
3. The simulated spread in debris energy is larger than $\Delta\epsilon = GM_{\text{bh}}/r_t(r_*/r_t)$ as the penetration factor increases for all cases, which is consistent with our assumption that the spread in debris energy is proportional to β^k (see also equation (4) of Stone et al. 2013). While the spread energy indexes k are distributed over $0.27 \lesssim k \lesssim 0.9$ for $n = 1.5$ case for any value of β and e , they are distributed over $0.97 \lesssim k \lesssim 1.58$ for $n = 3$ and any value of β and e except for the $\beta = 1.5$ case. In this case, k ranges from 2.08 to 2.17 depending on the orbital eccentricity.

4. The mass fallback rate becomes higher and its slope is steeper as the penetration factor increases in the early phase, while the slope is close to the standard rate $t^{-5/3}$ in the late time. We also find that the mass fallback rate can be about one order of magnitude higher and its slope steeper even in "marginally" eccentric TDEs ($e_{\text{crit},1} \lesssim e < 1.0$) than that of parabolic TDEs.
5. We find that the duration of the super-Eddington accretion phase is proportional to $\beta^{-3k/5}$ (see equation 22). Namely, the duration is shorter as the penetration factor is higher as far as k is positive. We have confirmed that this is consistent with the SPH simulation results. It demonstrates that the shorter duration can be evidence for the higher- β TDEs.
6. When the orbital eccentricity ranges for $1.0 < e < e_{\text{crit},2}$ (i.e., marginally hyperbolic TDEs), only a little fraction of stellar mass can fall back to the black hole, which leads to the formation of advection dominated accretion flow (ADAF) or radiatively inefficient accretion flows (RIAF). The marginally hyperbolic TDEs can be an origin of ADAFs (or RIAFs) around dormant SMBHs. If the orbital eccentricity is more than $e_{\text{crit},2}$ (i.e., hyperbolic TDEs), no stellar debris can fall back to the black hole, which leads to a failed TDE.

If $4 \lesssim \beta \lesssim \beta_{\text{max}}$, where $\beta_{\text{max}} = r_t/r_S \approx 24(M_{\text{bh}}/10^6 M_\odot)^{-2/3}(m_*/M_\odot)^{-1/3}(r_*/R_\odot)$ is the maximum value of the penetration factor, the general relativistic (GR) effects get significantly important. In this case, the spread in energy would not follow the simple power law of the penetration factor anymore. For example, if $\beta = 10$ and $k \sim 2$, we are not sure of whether the spread in energy can be 100 times larger than $\Delta\epsilon$ and also how high and steep in the early time the mass fallback rate is. We will examine how GR can affect on β -dependence of spread in energy in tidal disruption of such a deep-plunging star.

Hayasaki & Yamazaki (2019) proposed that high-energy neutrinos with \sim

$7.5 \text{ TeV} (M_{\text{bh}}/10^6 M_{\odot})^{5/3}$ can be emitted from an ADAF and/or RIAF formed after tidal disruption of a star by the decay of charged pions originated in ultra-relativistic protons. In the standard TDE theory, the RIAF phase would start at $t_{\text{RIA}} \sim 10^{10} \text{ s}$ for $10^6 M_{\odot}$ black hole after a solar-type star disruption. For marginally unbound TDEs, the RIAF phase would start at about four orders of magnitude earlier than the standard case, i.e., $t_{\text{RIA}} \sim 10^6 \text{ s}$ for $10^6 M_{\odot}$ black hole and a solar-type star. Because the neutrino energy generation rate is given by $L_{\nu} t_{\text{RIA}} \mathcal{R}$, where L_{ν} and \mathcal{R} are the neutrino luminosity and the TDE rate respectively, such a short timescale can significantly enhance the energy generation rate even if the event rate of marginally hyperbolic TDEs would be subdominant.

Acknowledgments

The authors thank Matthew Bate, Atsuo Okazaki, Takahiro Tanaka, and Nicholas C. Stone for their helpful comments and suggestions. This research has been supported by Basic Science Research Program through the National Research Foundation of Korea (NRF) funded by the Ministry of Education (2016R1A5A1013277 and 2017R1D1A1B03028580 to K.H.), and also supported by the National Supercomputing Center with supercomputing resources including technical support (KSC-2019-CRE-0082 to G.P. and K.H.).

REFERENCES

Alexander, K. D., Berger, E., Guillochon, J., Zauderer, B. A., & Williams, P. K. G. 2016, ApJ, 819, L25

Arcavi I. et al., 2014, ApJ, 793, 38

Auchettl, K., Guillochon, J., & Ramirez-Ruiz, E. 2017, ApJ, 838, 149

Bate, M. R., Bonnel, I. A., Price, N.M., 1995, MNRAS, 277, 362

Bate, M. R., 1995, Ph.D. Thesis, ch.2, 30-31

Benz W., 1990, in the Numerical Modeling of Nonlinear Stellar Pulsations: Problems and Prospects, ed. Buchler, R.J. (Dordrecht: Kluwer Academic Publishers), 269

Benz, W., Bowers, R.L., Cameron, A.G.W., Press, W.H., 1990, ApJ, 348, 647

Bonnerot, C. et al, 2016, MNRAS, 455, 2253

Brown, G. C., Levan, A. J., Stanway, E. R., et al. 2015, MNRAS, 452, 4297

Burrows D. N. et al., 2011, Nature 476, 421

Chornock, R., Berger, E., Gezari, S., et al. 2014, ApJ, 780, 44

Dai, L., McKinney, J. C., & Miller, M. C. 2015, ApJ, 812, L39

Donley J. L., Brandt W. N., Eracleous M., Boller T., 2002, AJ, 124, 1308

Evans C.R., Kochanek C.S., 1989, ApJ, 346, L13

Farrar, G. R., & Piran, T. 2014, arXiv:1411.0704

Gezari, S., Martin, D. C., Milliard, B., et al. 2006, ApJ, 653, L25

Gezari, S., Basa, S., Martin, D. C., et al. 2008, *ApJ*, 676, 944-969

Gezari S. et al., 2012, *Nature*, 485, 217

Guillochon, J., & Ramirez-Ruiz, E. 2013, *ApJ*, 767, 25

Hayasaki, K., Stone, N., Loeb, A. 2013, *MNRAS*, 434, 909

Hayasaki, K., Stone, N., Loeb, A. 2016, *MNRAS*, 461, 3760

Hayasaki, K., Zhong, S., Li, S., Spurzem R. 2018, *ApJ*, 855, 129

Hayasaki, K., & Yamazaki, R. 2019, *ApJ*, 886, 114

Holoién, T. W.-S., Prieto, J. L., Bersier, D., et al. 2014, *MNRAS*, 445, 3263

Holoién, T. W.-S., Kochanek, C. S., Prieto, J. L., et al. 2016, *MNRAS*, 455, 2918

Hung, T., Cenko, S. B., Roth, N., et al. 2019, arXiv e-prints , arXiv:1903.05637.

Komossa S., Bade N., 1999, *A&A*, 343, 775

Komossa, S. 2015, *Journal of High Energy Astrophysics*, 7, 148

Kormendy, J., Ho, L. C., 2013, *ARA&A*, 51, 511

Leloudas, G., Dai, L., Arcavi, I., et al. 2019, arXiv e-prints, arXiv:1903.03120

Lodato, G., King, A. R., & Pringle, J. E. 2009, *MNRAS*, 392, 332

Mainetti, D., Lapi, A., Campana, S., et al. 2017, *A&A*, 600, A124

MacLeod, M., Guillochon, J., & Ramirez-Ruiz, E. 2012, *ApJ*, 757, 134

Maksym, W. P., Ulmer, M. P., Eracleous, M. C., Guennou, L., & Ho, L. C. 2013, *MNRAS*, 435, 1904

Pasham, D. R., Remillard, R. A., Fragile, P. C., et al. 2018, arXiv e-prints , arXiv:1810.10713.

Phinney, E. S. 1989, in IAU Symp. 136, The Center of the Galaxy, ed. M. Morris (Dordrecht: Kluwer Academic Publishers), 543

Piran, T., Svirski, G., Krolik, J., Cheng, R. M., & Shiokawa, H. 2015, ApJ, 806, 164

Rees, M. J., 1988, Nature 333, 523

Saxton, R. D., Read, A. M., Esquej, P., et al. 2012, A&A, 541, A106

Shiokawa, H., Krolik, J. H., Cheng, R. M., Piran, T., & Noble, S. C. 2015, ApJ, 804, 85

Stone, N., Sari, R., & Loeb, A. 2013, MNRAS, 435, 1809

Stone, N., Metzger, B. D. 2016, MNRAS, 455, 859

van Velzen, S., Farrar, G. R., Gezari, S., et al. 2011, ApJ, 741, 73

van Velzen, S., Farrar, G. R., 2014, ApJ, 792, 53

van Velzen, S., Anderson, G. E., Stone, N. C., et al. 2016, Science, 351, 62

Wang, J., Merritt, D., 2004, ApJ, 600, 149

Zauderer B. A., et al., 2011, Nature 476, 425